JOURNAL OF AIRCRAFT
Vol. 48, No. 2, March–April 2011

Testing and System Identification of an Ornithopter in Longitudinal Flight

Jared Grauer,* Evan Ulrich,* James Hubbard Jr.,† Darryll Pines,‡ and J. Sean Humbert§
University of Maryland, College Park, Maryland 20742

DOI: 10.2514/1.C031208

There is currently a large effort underway to understand the flight dynamics of avian-based flapping-wing vehicles, or ornithopters, as they represent a critical intersection between existing biological flyers and the need for small aerial robots to conduct a variety of mission scenarios. Efforts to model the flight dynamics of these vehicles for feedback control have been complicated by a number of factors including nonlinear flight motions, unsteady aerodynamics at low Reynolds numbers, and limited sensor payload capacity. This paper presents data for a 0.45 kg ornithopter research platform, flown in straight and level mean flight. A visual tracking system was employed to follow retroreflective markers on the ornithopter and reconstruct state measurements. A multibody model of the flight dynamics was used to investigate the spatial distribution of kinematic variables over the duration of a wing stroke, and system identification techniques were employed to extract models for the lift, thrust, and pitching moment coefficients. Two methods of parameter estimation showed good results for relatively simple aerodynamic models that can be used for feedback control.

Nomenclature

$\mathbf{a}$	=	aerodynamic effects vector
$\mathbf{B}$	=	control effectiveness matrix
$\mathbf{C}$	=	dynamic coupling matrix
C_l, C_{ij}, C_0	=	reference frame location
C_L, C_T, C_m	=	aerodynamic coefficients
c	=	chord
f	=	frequency
$\mathbf{G}$	=	gear ratio matrix
$\mathbf{g}$	=	gravitational effects vector
$\mathbf{I}$	=	inertia tensor
$\mathbb{I}$	=	identity matrix
$\mathbf{J}_\eta$	=	orientation Jacobian matrix
$\mathbf{K}$	=	stiffness matrix
k	=	reduced frequency
L, M, T	=	lift, pitching moment, thrust
$\mathbf{M}$	=	mass matrix
$\mathbf{p}$	=	generalized position vector
$\mathbf{R}$	=	rotation matrix
Re	=	Reynolds number
$\Re$	=	real part
$\mathbf{r}$	=	position vector
$\boldsymbol{r}$, $\boldsymbol{l}$	=	joint locations
S	=	wing reference area
$S(.)$	=	skew operator
$s(.)$	=	standard error
$\mathcal{T}$	=	period
t	=	time
$\mathbf{u}$	=	control input vector
$\mathbf{v}$	=	generalized velocity vector
$\mathbf{X}$	=	regressor matrix
$\mathbf{z}$	=	measurement vector
α	=	angle of attack
δ, $\boldsymbol{\epsilon}$	=	quaternion scalar and vector parts
$\boldsymbol{\eta}$	=	orientation vector
$\boldsymbol{\theta}$	=	joint vector
μ	=	dynamic viscosity coefficient
$\boldsymbol{\nu}$	=	translational velocity
ρ	=	air density
$\boldsymbol{\phi}$	=	estimated parameters
$\boldsymbol{\omega}$	=	rotational velocity

Subscripts

$c/4$	=	quarter chord
mac	=	mean aerodynamic chord
x, y, z	=	orthogonal projections
$\|.\|_2$	=	Euclidean norm

Superscripts

T	=	transpose
†	=	complex conjugate transpose
-1	=	inverse
$\dot{}$	=	time derivative
$\hat{}$	=	estimated value

I. Introduction

ORNITHOPTERS are aerial flight vehicles that use flapping wings to produce lift and thrust forces in a manner similar to birds and bats. Although progress has been made with manned versions [1], the most prevalent ornithopters are unmanned air vehicles with mass ranging between a few grams to a kilogram. Flapping-wing aircraft represent a unique paradigm in the spectrum of available unmanned aerial systems. As vehicles are made smaller, fixed- and rotary-wing aircraft suffer from Reynolds effects, whereas flapping-wing vehicles enjoy aerodynamic benefits [2–4]. The ornithopter represents a safe, agile, and robust platform, capable of carrying useful sensor payloads while conducting unmanned mission scenarios. It is envisioned that the ornithopter will contribute to such civilian applications as crop surveying, weather data collection, wildlife population monitoring, and search and rescue, as well as military applications including perimeter surveillance, reconnaissance, and chemical plume detection.

Received 9 August 2010; revision received 15 November 2010; accepted for publication 15 November 2010.

*Graduate Student, Department of Aerospace Engineering. Member AIAA.
†Langley Distinguished Professor, Department of Aerospace Engineering. Associate Fellow AIAA.
‡Dean and Professor, Department of Aerospace Engineering. Fellow AIAA.
§Assistant Professor, Department of Aerospace Engineering. Member AIAA.

A parsimonious model of the flight dynamics is needed to design the requisite feedback control laws to mature to the ornithopter into an autonomous vehicle for effective mission deployment. However, difficulties arise in modeling both the aerodynamics and the vehicle dynamics of the ornithopter. The aerodynamics are challenging to model due to three dimensional, unsteady fluid flows that occur at low Reynolds numbers [2]. Computational fluid dynamics codes are able to illuminate the fundamental flow physics [5,6], but are currently too large to use for feedback control design. First principles models have been developed for both insect-based flappers [7,8] and avian-based flappers [9]; however, these models often represent highly simplified descriptions of the aerodynamic environment. Wind tunnel tests have been conducted where the ornithopter is mounted on a sting that measures lift and thrust forces for a variety of freestream conditions [6,10,11]. However, this method constrains the natural bounding motion of the ornithopter and changes the aerodynamics experienced in flight. The vehicle dynamics, due to nonlinear motions observed in flight [12] and a variable mass distribution, require nonlinear multibody models to model [13–16]. This creates a more complex model and requires a more advanced stability analysis [17,18].

An alternative approach is to use system identification techniques with data collected during a flight test to determine an aerodynamic model [19,20]. Knowledge of a rigid body model facilitates the computation of aerodynamic forces and moments on the system, with which model structure determination and parameter estimation routines can be employed to extract the model. This method can be cheaper than wind tunnel testing and typically provides more realistic results [20].

In this work an ornithopter flight test is presented where a visual tracking system has been employed to measure state variables. This method is a low-noise, minimally-invasive measurement which has been successfully employed in the past to control multiple vehicles and conduct system identification [21,22]. A multibody model of the flight dynamics previously developed [15] is leveraged to investigate the spatial distribution of kinematic variables over the duration of a wing stroke and to facilitate the system identification of an aerodynamic model in longitudinal flight. Section II describes the experimental aircraft, and Sec. III reviews the multibody model of the flight dynamics. Section IV describes the experimental setup, and Sec. V presents the flight data, spatial distributions of kinematic variables, and system identification of the wing aerodynamics model.

II. Aircraft Description

This work was performed using the flapping-wing research platform pictured in Fig. 1. After flying several commercially available ornithopters, this Kinkade Slow Hawk ornithopter was selected due to adequate flight performance, relative ease of piloting, robustness to wind gusts and hard landings, and available sensor payload capacity.

The ornithopter is flown similarly to other hobby aircraft: a pilot launches the vehicle into the air and uses a radio transmitter to relay joystick commands to an onboard receiver, which directs power from a lithium polymer battery to the actuators. The throttle input commands a Feigao direct current brushless motor that drives a four-bar linkage to flap the wings, creating lift and thrust forces. Two additional joystick inputs command two serially arranged Hitec HS-56 servo motors that pitch and roll the tail to create pitching and yawing aerodynamic control torques.

Fig. 1 Ornithopter test aircraft.

The ornithopter fuselage is cut from a single 3 mm ply of carbon fiber and has affixed the onboard electrical components. The nose of the ornithopter has been reinforced with additional carbon fiber plies for structural robustness. The wings and tail are membrane sails constructed of rip-stop polyester, dacron tape, and carbon fiber spars. The wings have a 1.2 m span, a 0.4 m depth, a 0.3 m^2 area, and a 4.4 aspect ratio. The tail has a 0.2 m span, 0.2 m length, 0.04 m^2 area, and a 1.5 aspect ratio.

Unlike conventional aircraft, the ornithopter has several moving parts that significantly impact the mass distribution of the vehicle. The fuselage constitutes 76.5% of the total 0.45 kg mass, whereas the wings and tail comprise 18.6 and 4.9%, respectively. Inertia tensors were computed using weight measurements and a CAD program that constructed three dimensional objects from a series of photographs. Figure 2 shows the migration of the center of mass and respective inertia tensor for the gross vehicle as the wings rotate. The vertical position of the center of mass and the moments of inertia experience significant variations that impact the flight dynamics of the ornithopter.

III. Flight Dynamics Model

Fast motions observed in flight [12] and large mass variations occurring at frequencies near the expected rigid body modes has led to the development of a nonlinear multibody model of the ornithopter flight dynamics [15]. The ornithopter is approximated as a system of five rigid bodies, illustrated in Fig. 3, consisting of the fuselage, two wings, and two tail components.

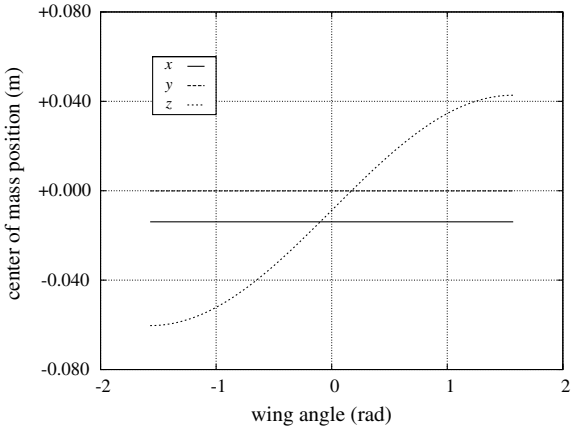

a) Center of mass location

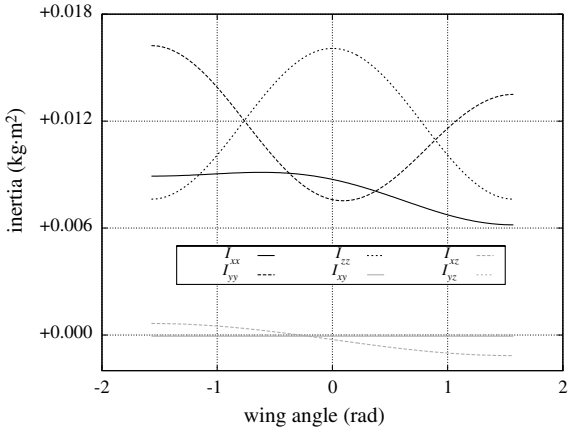

b) Inertia tensor

Fig. 2 Variation of mass distribution with wing angle.

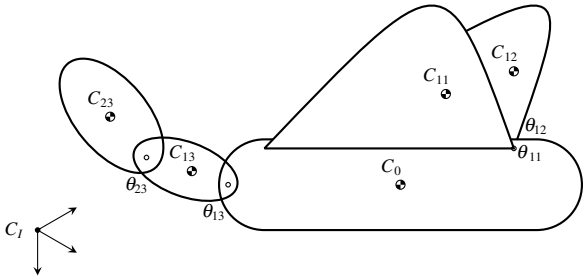

Fig. 3 Multibody ornithopter model schematic.

The position states are

$$\mathbf{p} = \begin{bmatrix} \mathbf{r}^I_{0,I} \\ \boldsymbol{\eta}^I_{0,I} \\ \boldsymbol{\theta} \end{bmatrix} \tag{1}$$

where $\mathbf{r}^I_{0,I}$ is the inertial position of the fuselage center of mass, $\boldsymbol{\eta}^I_{0,I}$ is a quaternion describing the orientation of the fuselage, having scalar part δ and vector part $\boldsymbol{\epsilon}$, and $\boldsymbol{\theta}$ is a vector concatenating the articulated joint angles of the ornithopter. The generalized velocity states are

$$\mathbf{v} = \begin{bmatrix} \boldsymbol{v}^0_{0,I} \\ \boldsymbol{\omega}^0_{0,I} \\ \dot{\boldsymbol{\theta}} \end{bmatrix} \tag{2}$$

where $\boldsymbol{v}^0_{0,I}$ and $\boldsymbol{\omega}^0_{0,I}$ are the body-fixed translational and rotational velocities of the fuselage, and where $\dot{\boldsymbol{\theta}}$ are the joint rates.

The kinematic equations describe the evolution of the position states as a function of the velocity states and are written

$$\begin{bmatrix} \dot{\mathbf{r}}^I_{0,I} \\ \dot{\boldsymbol{\eta}}^I_{0,I} \\ \dot{\boldsymbol{\theta}} \end{bmatrix} = \begin{bmatrix} \mathbf{R}^{I,0} & \mathbf{0} & \mathbf{0} \\ \mathbf{0} & \mathbf{J}^{I,0}_{\eta} & \mathbf{0} \\ \mathbf{0} & \mathbf{0} & \mathbb{I} \end{bmatrix} \begin{bmatrix} \boldsymbol{v}^0_{0,I} \\ \boldsymbol{\omega}^0_{0,I} \\ \dot{\boldsymbol{\theta}} \end{bmatrix} \tag{3}$$

where

$$\mathbf{R}^{I,0} = (\delta^2 - \boldsymbol{\epsilon}^T\boldsymbol{\epsilon})\mathbb{I} + 2\boldsymbol{\epsilon}\boldsymbol{\epsilon}^T + 2\delta S(\boldsymbol{\epsilon}) \tag{4}$$

is a rotation matrix, $S(.)$ is a skew operator defined for any three-element vector as

$$S(\boldsymbol{\epsilon}) = \begin{bmatrix} 0 & -\epsilon_3 & \epsilon_2 \\ \epsilon_3 & 0 & -\epsilon_1 \\ -\epsilon_2 & \epsilon_1 & 0 \end{bmatrix} \tag{5}$$

and

$$\mathbf{J}^{I,0}_{\eta} = \frac{1}{2}\begin{bmatrix} \delta\mathbb{I} - S(\boldsymbol{\epsilon}) \\ -\boldsymbol{\epsilon}^T \end{bmatrix} \tag{6}$$

is an orientation Jacobian matrix.

The dynamic equations describe the evolution of the ornithopter velocity states as a function of the position, velocity, and control input. The Boltzmann–Hamel equations were applied to derive the dynamic equations in the form

$$\mathbf{M}\dot{\mathbf{v}} + \mathbf{Cv} + \mathbf{Gg} + \mathbf{Ga} + \mathbf{Kp} = \mathbf{Bu} \tag{7}$$

where $\mathbf{u}$ represents the pilot control inputs. The matrix $\mathbf{M}$ represents the generalized mass and inertia of the system; $\mathbf{C}$ contains Coriolis and centripetal forces, as well as damping terms in the actuators; $\mathbf{G}$ is a matrix of gear ratios; $\mathbf{g}$ and $\mathbf{a}$ are the effects due to gravitational and aerodynamic forces; $\mathbf{K}$ contains stiffness terms in the servo motors; and $\mathbf{B}$ represents the control effectiveness matrix. Wind tunnel tests have been performed to model the aerodynamic effects of the tail [23] and system identification techniques were applied to model the dynamics of the onboard actuators [24].

IV. Experimental Setup

A. Visual Tracking System

A Vicon visual tracking system was used to observe the ornithopter in flight. This system provides minimally-invasive, low-noise, high-fidelity measurements, and has been successfully employed to control groups of unmanned vehicles [21] and perform system identification [22]. The ornithopter was outfitted with several retro-reflective markers. The spatial position of these markers was estimated using supplied software, which combined planar images from eight strobing cameras in a least-squares fashion.

Flight testing was performed in a 33.5 m long indoor corridor, as illustrated in Fig. 4, to reduce the effects of gust disturbances and to minimize erroneous optical reflections to the camera system. The cameras were placed at the corners of a capture volume 10 m long, 6 m wide, and 5 m tall. This camera configuration was found to represent a good compromise between competing requirements to have a large capture volume in which to take data, and a small capture volume to achieve good measurement accuracy.

The configuration of markers on the vehicle determines the quality of data extracted from the flight test. Better performance is obtained by using more and larger markers, however, this also begins to impact the flight dynamics and the visual tracking system has problems distinguishing markers at further distances. The marker configuration used in the flight test is pictured in Fig. 5. Three spherical markers of diameter 10 mm and mass 1 g were placed around the nose of the aircraft, which was the most visible and least flexible portion of the fuselage. Each wing had retroreflective tape placed along the leading edge spar at wing tip and one third span, as well as along the secondary wing spar, as these were the most rigid sections on the ornithopter wing. Markers were attached to the center and sides of the tail. This configuration yielded a standard errors of 1.3 mm and represented a good configuration for extracting rigid body information. Additional markers and other marker locations were attempted but the visual tracking system had problems distinguishing the markers. Measurement accuracy could be improved using a combination of more markers with more cameras placed closer to the flight path.

B. Testing Procedure

Flight tests were performed indoors and measures were taken to conduct safe and repeatable flight tests. A low-friction guide wire made from monofilament fishing line with 80 lb capacity was stretched taught over the length of the corridor. A second line connected the ornithopter nominal center of mass to the guide line and was long enough that it was loose when the ornithopter was not

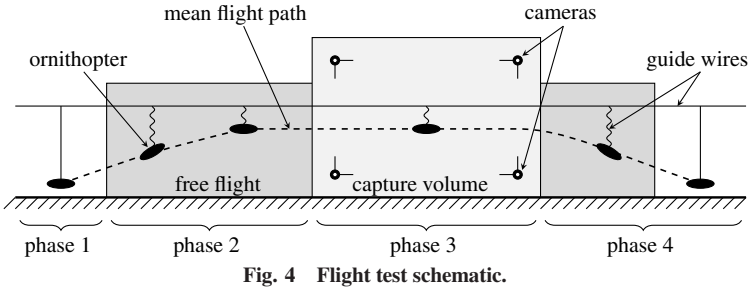

Fig. 4 Flight test schematic.

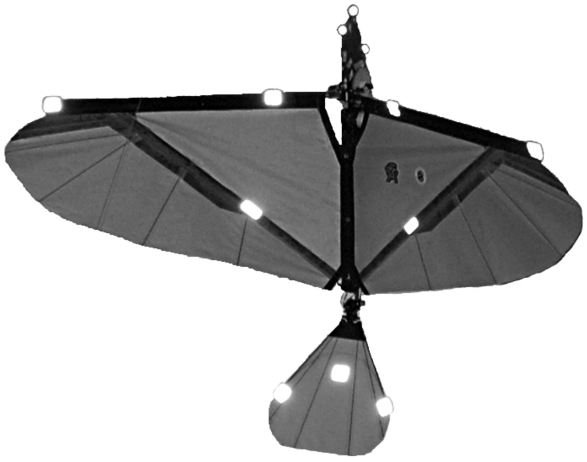

Fig. 5 Ornithopter fitted with retroreflective markers.

resting on the ground. This configuration both restrained the ornithopter from dangerous flight excursions and enabled free-flight conditions with only a minimal amount of drag and friction added by the lines. This configuration also allowed for tests to start from a resting position, which led to more controlled and repeatable tests than from the normal hand launching procedure.

The experimental flight tests consisted of four phases, also illustrated in Fig. 4. First the ornithopter began flapping from rest with the tail set at its minimum deflection setting, allowing the ornithopter to quickly gather speed with minimal drag. In the second phase the longitudinal tail control was used to trim the ornithopter for straight and level flight at a free-flying altitude. The third phase was trimmed flight through the capture volume while recording visual tracking data. The final phase consisted of decelerating the ornithopter upon exiting the capture volume.

C. Data Postprocessing

Marker position data was recorded at 500 Hz. A low-pass smoothing filter [20] with a 50 Hz cutoff frequency was applied to the data afterwards to attenuate measurement noise. The marker locations were then used to estimate the position and orientation of rigid bodies representing the fuselage, wings, and tail. The marker positions on a rigid body are illustrated in Fig. 6 and can be expressed as

$$\mathbf{r}^{\,I}_{k,I} = \mathbf{r}^{I}_{ij,I} + \mathbf{R}^{I,ij}\mathbf{r}^{ij}_{k,ij} \tag{8}$$

where $\mathbf{r}^{I}_{k,I}$ is the position of the kth marker on rigid body ij, expressed in the inertial frame, and $\mathbf{r}^{ij}_{k,ij}$ is the known marker location of the kth marker on rigid body ij, relative to its center of mass. Visual tracking system data $\mathbf{r}^{I}_{k,I}$ and measurements of $\mathbf{r}^{ij}_{k,ij}$ were supplied to the MATLAB function *fminsearch*, which estimated the position $\mathbf{r}^{I}_{ij,I}$ and orientation $\boldsymbol{\eta}^{I}_{ij,I}$ of each rigid body with mean standard errors of 0.98 mm in position and 0.0043 rad in orientation.

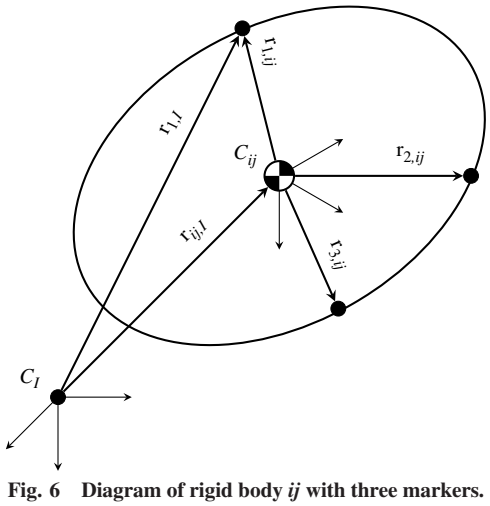

Fig. 6 Diagram of rigid body *ij* with three markers.

Kinematic relations were then used to compute the position state variables in Eq. (1) from the rigid body position and orientation data. Position data obtained in this method had sufficient noise levels to permit smooth numerical differentiation [20] to yield the velocity states through the inverse relation of Eq. (2).

V. Experimental Results

A. State Measurements

A data set displaying the longitudinal state variables in straight and level mean flight is shown in Fig. 7, where r_x and v_x are the forward position and velocity, r_z and v_z are the heave position and velocity, θ and ω_y are the pitch angle and pitch rate, θ_{11} and $\dot{\theta}_{11}$ are the angular position and velocity of the right wing relative to the fuselage, and θ_{14} and $\dot{\theta}_{14}$ are the relative longitudinal tail pitch angle and pitch rate. Approximately three flapping cycles of data are shown, having a $\mathcal{T} = 0.17$ s period or a 5.91 Hz flapping frequency. The flight was conducted with 77% throttle, -0.12 rad of elevator, and -0.06 rad of rudder.

The ornithopter is accelerating slightly, but has a mean forward velocity of 9.2 m/s. The down stroke phase of the flapping cycle has deflection extrema -0.67 and $+0.39$ rad, and occurs from $0.24\mathcal{T}$ to $0.78\mathcal{T}$, yielding a down stroke to up stroke ratio of 1.18. This stroke differential is smaller than for similarly sized birds and indicates a relative inefficiency in creating thrust forces [25]. The cyclic forcing of the wings induces a heave velocity between -1.1 and 0.9 m/s, which results in a 0.08 m oscillation about the nominal 0.9 m altitude. Smooth numerical differentiation of the heave velocity yielded translational acceleration between -4.0 and $+4.9$ times the acceleration of gravity at the fuselage center of mass of the fuselage, consistent with previous accelerometer measurements [12]. The cyclic forcing of the wings also induces a pitch rate ranging between -1.4 and $+1.6$ rad/s, resulting in a 0.02 rad oscillation about the mean pitch angle. These heave and pitch motions are fast and large amplitude, compared with conventional aircraft flying in steady conditions. The longitudinal deflection of the tail relative to the fuselage θ_{14}, although set to the trim value, is not constant and changes due to reaction forces generated by the wings on the fuselage.

B. Kinematic Analysis

The state measurements and rigid body model facilitate an investigation into the spatial distribution of kinematic variables over the duration of a wing stroke. These distributions are shown in Fig. 8 as polar plots, where the angular coordinate indicates the temporal position within the wing stroke, where $(0/4)\mathcal{T}$ is wings level, $(1/4)\mathcal{T}$ is wings up, $(2/4)\mathcal{T}$ is wings level, and $(3/4)\mathcal{T}$ is wings down. The radial coordinate indicates the spatial position along the wing, where the center and circumference of the circle correspond to the wing root and wing tip, respectively. A discretization using 75 spatial elements along the wing span and 200 temporal points through the wing stroke was used to generate these figures.

It is well known that aeroelastic effects play an important role in the aerodynamic response of flapping wings [26] and it has been suggested in previous wing shape experiments that leading edge spar deformations can impact the aerodynamics [27]. Figure 8a shows the deformations of the leading edge spar, which is taken as the difference between the rigid spar, measured using the wing hinge location and the one-third-span marker location, and the deformed spar, measured using the wing hinge location, the one-third-span marker location, and the full-span marker location. The tips experience maximum deflections of -0.02 and $+0.01$ m, at $0.13\mathcal{T}$ after transitions between up and down strokes. The difference in deflection amounts are due to gravity and increased aerodynamic loads in the down stroke. The relatively small deflections in this flight

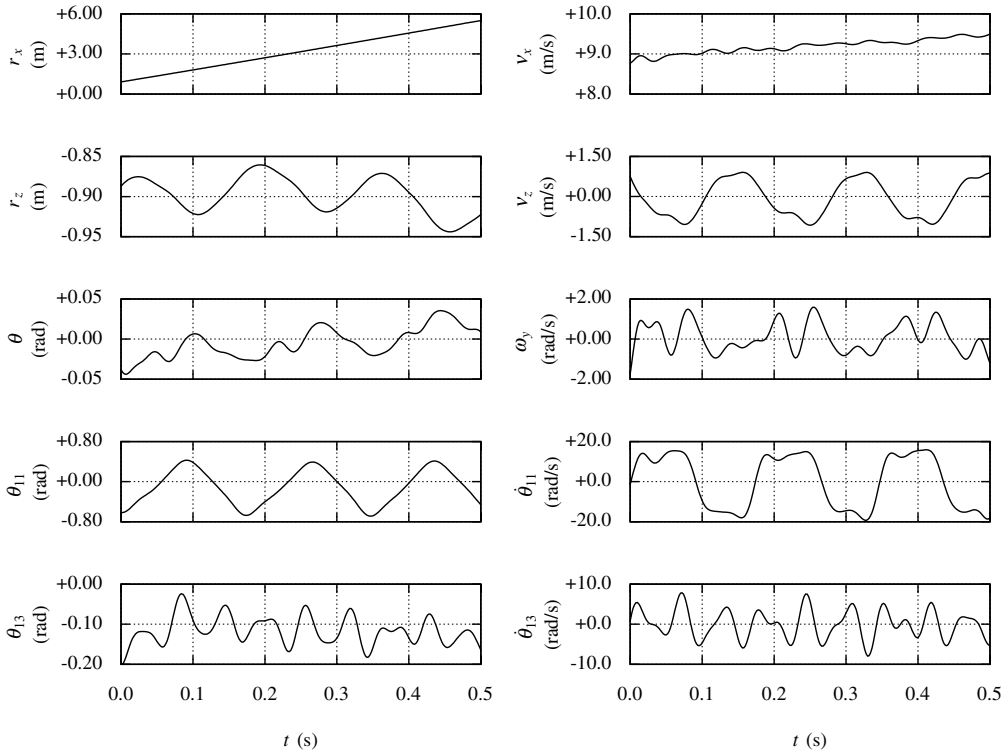

Fig. 7 State measurements extracted from flight data.

indicate that leading edge spar deformations for this ornithopter are not expected to cause large effects.

The translational velocity of each wing section at the local quarter chord, shown in Fig. 8b, is

$$\boldsymbol{v}_{c/4} = \boldsymbol{v}_{0,I} + S(\boldsymbol{\omega}_{0,I})\boldsymbol{r}_{01} + S(\boldsymbol{\omega}_{0,I} + \mathbf{Z}_{11}\dot{\boldsymbol{\theta}})(\boldsymbol{r}_{c/4,11} - \boldsymbol{l}_{11}) \quad (9)$$

where $\boldsymbol{r}_{01}$ is the distance from the fuselage center of mass to the wing hinge, $\boldsymbol{l}_{11}$ is the distance from the wing center of mass to the wing hinge, $\boldsymbol{r}_{c/4,11}$ is the distance from the wing center of mass to the local quarter chord, and $\mathbf{Z}_{11}$ is a matrix which extracts the wing angle. The velocity magnitude has a minimum value of 8.9 m/s due to the forward motion, and a maximum velocity of 11.0 m/s at the wing tips due to additional rotational motion of the wings and fuselage. Skewness in this plot is a result the ornithopter pitch rate profile and the wing stroke profile admitted by the four-bar linkage assembly.

The angle of attack is the primary variable used for parameterizing aerodynamic forces. Flapping-wing vehicles routinely

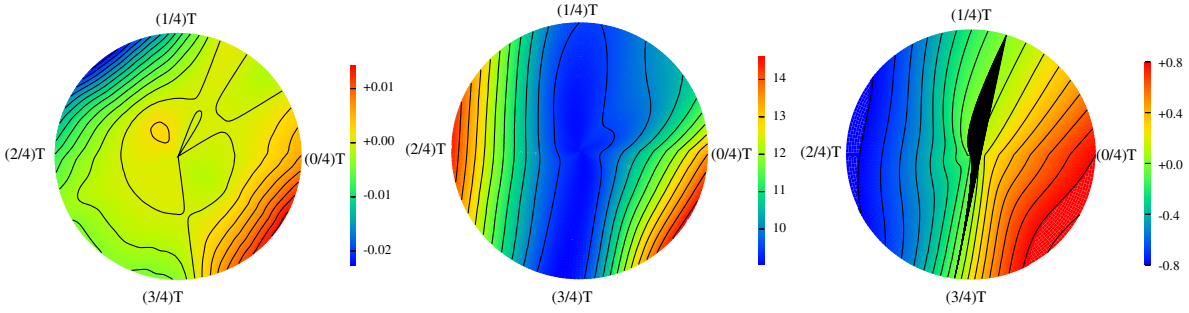

a) Wing deformations (m) **b) Velocity magnitude (m/s)** **c) Angle of attack (rad)**

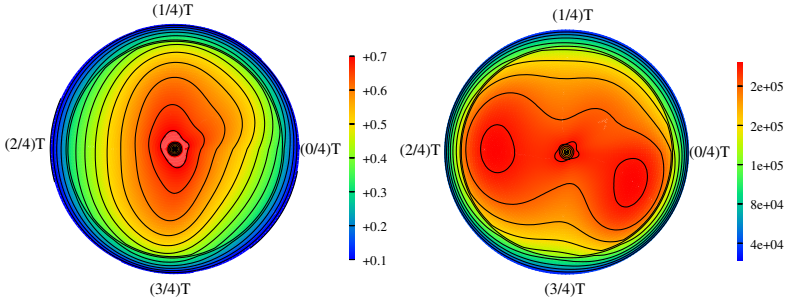

d) Reduced frequency **e) Reynolds number**

Fig. 8 Scalar distributions over a wing stroke.

experience flight at large local angles of attack an incur complex phenomenon such as dynamic stall. The angle of attack at the local quarter chord, shown in Fig. 8c can be computed from the translational velocities as

$$\alpha_{c/4} = \arctan\left(\frac{v_{c/4,z}}{v_{c/4,x}}\right) \tag{10}$$

where the additional subscripts denote the velocity component. Ranging between -0.94 and $+0.86$ rad, the angle of attack goes through very high variations on each wing stroke.

Reduced frequency, which is related to the Strouhal number, is a measure of the unsteadiness of the airflow, and is defined as

$$k = \frac{\pi f c}{\|\boldsymbol{v}_{c/4}\|_2^2} \tag{11}$$

where f is the flapping frequency and c is the blade element chord length. The reduced frequency distribution illustrated in Fig. 8d varies between 0.0458 and 0.7404, which are considered highly unsteady [28].

The Reynolds number is the ratio of inertial to viscous forces and is important for flapping-wing vehicles because it is low-Reynolds-number aerodynamics where flapping-wing vehicles become more efficient and where the aerodynamic forces become more difficult to model. The local Reynolds number along the wing span is

$$Re = \frac{\rho c \|\boldsymbol{v}_{c/4}\|_2}{\mu} \tag{12}$$

where ρ is the air density, c is the local chord length, and μ is the dynamic viscosity coefficient. The Reynolds numbers are small near the root and tip of the ornithopter wing, where the chord length becomes very small, and larger towards the center portion of the wing, where the flow experiences larger velocities and chord lengths. The Reynolds number ranges from 19,000 to 232,000 for this flight.

C. Dynamic Analysis

The aerodynamic contribution of the wing is the only unknown term in Eq. (7), which can be partitioned and solved for as

$$\mathbf{a}_{\text{wing}} = \frac{1}{2}\mathbf{G}^{-1}[\mathbf{Bu} - \mathbf{M}\dot{\mathbf{v}} - \mathbf{Cv} - \mathbf{Gg} - \mathbf{Kp}] - \frac{1}{2}\mathbf{a}_{\text{tail}} \tag{13}$$

Substitution of state measurements from the flight test into Eq. (13) yield measurements of the aerodynamic forces on the wing. The lift, thrust, and pitching moments are nondimensionalized as

$$C_L = 2L/\rho S\|\boldsymbol{v}_{\text{mac}}\|_2^2 \tag{14}$$

$$C_T = 2T/\rho S\|\boldsymbol{v}_{\text{mac}}\|_2^2 \tag{15}$$

$$C_m = 2M/\rho Sc\|\boldsymbol{v}_{\text{mac}}\|_2^2 \tag{16}$$

where ρ is the air density, S is the planform area, and $\boldsymbol{v}_{\text{mac}}$ is the velocity at the wing mean aerodynamic center.

System identification was applied to determine a model structure for the aerodynamic coefficients and to estimate the parameters within that model. Stepwise regression [20,29], a process where candidate regressors are iteratively swapped in and out of the model based on a palette of statistical metrics, was performed in the time domain and resulted in the model structure

$$C_L = C_{L_0} + C_{L_{v_x}} v_x + C_{L_{v_z}} v_z + C_{L_{\omega_y}} \omega_y + C_{L_{\dot{\theta}_{11}}} \dot{\theta}_{11} \tag{17}$$

$$C_T = C_{T_0} + C_{T_{\dot{\theta}_{11}}} \dot{\theta}_{11} + C_{T_{\theta_{11}^2}} \theta_{11}^2 + C_{T_{\dot{\theta}_{11}^2}} \dot{\theta}_{11}^2 \tag{18}$$

$$C_m = C_{m_0} + C_{m_{\omega_y}} \omega_y + C_{m_{\dot{\theta}_{11}}} \dot{\theta}_{11} \tag{19}$$

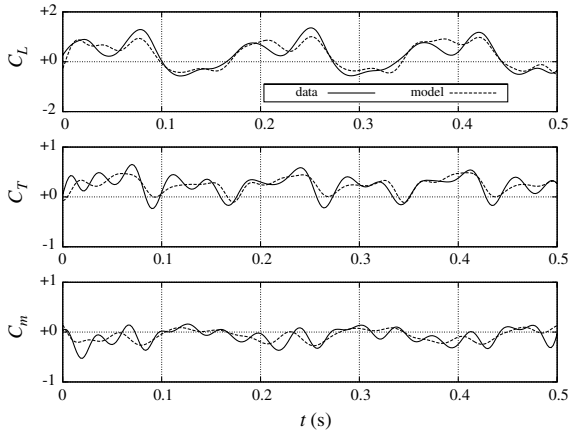

a) Time domain

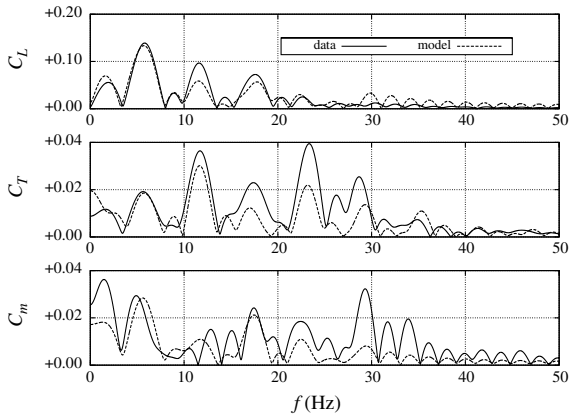

b) Frequency domain

Fig. 9 Model fits using equation error.

The lift model is essentially a quasi-steady model, commonly used to describe flapping-wing flight dynamics [7,9]. The thrust model captures profile drag, instantaneous drag, and two-per-flap thrust contributions. The pitching moment model captures contributions due to pitch rate and wing speed.

Each of the Eqs. (17–19) forms a linear least-squares estimation problem of the form

$$\mathbf{z} = \mathbf{X}\boldsymbol{\phi} \tag{20}$$

where, given measurements of the aerodynamic coefficients $\mathbf{z}$ and a set of regressors $\mathbf{X}$, the unknown model parameters can be solved for as

Table 1 Wing aerodynamic parameter estimation results

Parameter, ϕ	Time domain, $\hat{\phi} + s(\hat{\phi})$	Frequency domain, $\hat{\phi} + s(\hat{\phi})$
C_{L_0}	-1.5507 ± 1.7051	-1.7728 ± 1.1093
$C_{L_{v_x}}$	$+0.1966 \pm 0.0185$	$+0.3421 \pm 0.0067$
$C_{L_{v_z}}$	$+0.0575 \pm 0.0096$	$+0.2081 \pm 0.0066$
$C_{L_{\omega_y}}$	$+0.2540 \pm 0.0968$	$+0.3418 \pm 0.0056$
$C_{L_{\dot{\theta}_{11}}}$	$+0.0311 \pm 0.0040$	$+0.0371 \pm 0.0003$
C_{T_0}	-0.0734 ± 0.0068	-0.0811 ± 0.0039
$C_{T_{\dot{\theta}_{11}}}$	-0.0068 ± 0.0010	-0.0066 ± 0.0002
$C_{T_{\theta_{11}^2}}$	$+0.3760 \pm 0.1388$	$+0.1271 \pm 0.0153$
$C_{T_{\dot{\theta}_{11}^2}}$	-0.0012 ± 0.0003	-0.0013 ± 0.0000
C_{m_0}	-0.0587 ± 0.0098	-0.0579 ± 0.0091
$C_{m_{\omega_y}}$	-0.1132 ± 0.0399	-0.1333 ± 0.0033
$C_{m_{\dot{\theta}_{11}}}$	-0.0029 ± 0.0018	-0.0025 ± 0.0002

$$\hat{\boldsymbol{\phi}} = [\Re(\mathbf{X}^{\dagger}\mathbf{X})^{-1}]\Re(\mathbf{X}^{\dagger}\mathbf{z}) \tag{21}$$

Estimation was performed in both the time and frequency domains, with model fits to data shown in Fig. 9. The model captures much of the content. The estimated parameters are given in Table 1 along with standard errors, corrected for colored residuals [20]. Generally the estimates are consistent between the two domains in which the estimation was performed. The frequency domain results typically have smaller error bounds than in the time domain, indicating better results. There is some disagreement on the value of the lift contribution with respect to the vertical velocity, as the estimates are different with similar errors bounds. This could be in part because the heave velocity is much less in magnitude than the longitudinal velocity.

VI. Conclusions

In this paper an flight test was presented where the ornithopter was flown in straight and level mean flight through an indoor corridor, and state variables were reconstructed through measurements obtained using a visual positioning system. A multibody model of the flight dynamics, developed to capture the fast motions and pose-dependent mass distribution, was presented and used to compute the spatial distribution of kinematic variables through a wing stroke. Lastly, system identification techniques were employed to extract models for the longitudinal aerodynamic forces and torques.

Experimental testing of ornithopters is difficult because conventional wind tunnel testing constrains the natural flight motions of the ornithopter and standard avionics packages are not able to provide accurate state estimates. This work presents a method of testing ornithopters that permits free flight and uses a visual tracking system to obtain state measurements. A setup using eight cameras and 12 markers on the ornithopter produced good results with a sufficient resolution. However the capture volume was only large enough that three wing strokes of data could be captured. A larger flight area with more cameras and larger and more markers would yield good results with longer flight durations.

State measurements from the flight test data showed similar trends and oscillations to those measured previously using an inertial measurement unit. Spatial distributions of kinematic variables over the wing stroke revealed things about the flight of the ornithopter. For instance with this ornithopter, bending of the leading edge spar is not expected to significantly affect the aeroelastic effects, as deformations were relatively small. The ornithopter experiences large variations of velocity and angle of attack indicating the need for blade element models and poststall modeling to achieve high-fidelity modeling accuracy. The range of Reynolds number exists in the transition range where the shrinking size creates inefficiencies in creating lift and thrust. Future ornithopter designs could design the wings to operate in slightly larger Reynolds numbers to achieve higher control authority and efficiency.

System identification was applied to extract aerodynamic models for the longitudinal forces and moments acting on the wings from flight data. Model structure determination produced relatively low-order models in simple expansions of the states that well approximate the aerodynamic forces and can be used to design controllers. Two sets of parameter estimates showed good agreement between the estimated parameters and uncertainty bounds.

Acknowledgments

Funding for this work was supplied by the Army Micro Autonomous Systems and Technology Collaborative Technology Alliance. The authors wish to acknowledge the University of Maryland, the National Institute of Aerospace, and the NASA Langley Research Center for their support in this research. Flight tests were conducted at the University of Maryland. The authors would additionally like to thank the members of the Morpheus Laboratory and the Autonomous Flight Laboratory for their continued teamwork and motivation.

References

[1] DeLaurier, J., "An Ornithopter Wing Design," *Canadian Aeronautics and Space Journal*, Vol. 40, No. 1, March 1994, pp. 10–18.

[2] Mueller, T. (ed.), *Fixed and Flapping Wing Aerodynamics for Micro Air Vehicle Applications*, AIAA, Reston, VA, 2001, pp. 1–9.

[3] Seshadri, P., Benedict, M., and Chopra, I., "Experimental Investigation of an Insect-Based Flapping Wing Hovering Micro Air Vehicle," Aeromechanics Specialists Conference, American Helicopter Society, San Francisco, CA, Jan. 2010.

[4] Pesavento, U., and Wang, Z., "Flapping Wing Flight Can Save Aerodynamic Power Compared to Steady Flight," *Physical Review Letters*, Vol. 103, No. 11, Sept. 2009, pp. 1–4.

[5] Shyy, W., Lian, Y., Tang, J., Viieru, D., and Liu, H., *Aerodynamics of Low Reynolds Number Flyers*, Cambridge Aerospace Series, Cambridge Univ. Press, Cambridge, England, U.K., 2007, pp. 101–157.

[6] Roget, B., Sitaraman, J., Harmon, R., Grauer, J., Hubbard, J., and Humbert, S., "Computational Study of Flexible Wing Ornithopter Flight," *Journal of Aircraft*, Vol. 46, No. 6, Nov.–Dec. 2009, pp. 2016–2031.
doi:10.2514/1.43187

[7] Sane, S., and Dickinson, M., "The Aerodynamic Effects of Wing Rotation and a Revised Quasi-Steady Model of Flapping Flight," *Journal of Experimental Biology*, Vol. 205, 2002, pp. 1087–1096.

[8] Berman, G., and Wang, Z., "Energy-Minimizing Kinematics in Hovering Insect Flight," *Journal of Fluid Mechanics*, Vol. 582, 2007, pp. 153–168.
doi:10.1017/S0022112007006209

[9] DeLaurier, J., "An Aerodynamic Mode for Flapping-Wing Flight," *Aeronautical Journal*, No. 1853, April 1993, pp. 125–130.

[10] Park, J., and Yoon, K., "Designing a Biomimetic Ornithopter Capable of Sustained and Controlled Flight," *Journal of Bionic Engineering*, Vol. 5, No. 1, 2008, pp. 39–47.

[11] Krashanitsa, R., Silin, D., Shkarayev, S., and Abate, G., "Flight Dynamics of a Flapping-Wing Air Vehicle," *International Journal of Micro Air Vehicles*, Vol. 1, No. 1, 2009, pp. 35–49.

[12] Grauer, J., and Hubbard, J., "Inertial Measurements from Flight Data of a Flapping-Wing Ornithopter," *Journal of Guidance, Control, and Dynamics*, Vol. 32, No. 1, Jan.–Feb. 2009, pp. 326–331.
doi:10.2514/1.37495

[13] Rashid, T., "The Flight Dynamics of a Full-Scale Ornithopter," Master's Thesis, Univ. of Toronto, Toronto, 1995.

[14] Sibilski, K., "Dynamics of Micro-Air-Vehicle with Flapping Wings," *Acta Polytechnica Scandinavica, Mechanical Engineering Series*, Vol. 44, No. 2, 2004, pp. 15–21.

[15] Grauer, J., and Hubbard, J., "Multibody Model of an Ornithopter," *Journal of Guidance, Control, and Dynamics*, Vol. 32, No. 5, Sept.–Oct. 2009, pp. 1675–1679.
doi:10.2514/1.43177

[16] Bolender, M., "Rigid Multi-Body Equations-of-Motion for Flapping Wing MAVs Using Kane's Equations," AIAA Guidance, Navigation, and Control Conference, Chicago, IL, AIAA Paper 2009-6158, Aug. 2009.

[17] Dietl, J., and Garcia, E., "Stability in Ornithopter Longitudinal Flight Dynamics," *Journal of Guidance, Control, and Dynamics*, Vol. 31, No. 4, July–Aug. 2008, pp. 1157–1162.
doi:10.2514/1.33561

[18] Bolender, M., "Open-Loop Stability of Flapping Flight in Hover," AIAA Guidance, Navigation, and Control Conference, Toronto, AIAA Paper 2010-7552, Aug. 2010.

[19] Abdulrahim, M., Garcia, H., Ivey, G., and Lind, R., "Flight Testing a Micro Air Vehicle Using Morphing for Aeroservoelastic Control," AIAA Structural Dynamics and Materials Conference, Palm Springs, CA, AIAA Paper 2004-1674, April 2004.

[20] Klein, V., and Morelli, E., *Aircraft System Identification: Theory and Practice*, AIAA, Reston, VA, 2006, pp. 95–295.

[21] How, J., Bethke, B., Frank, A., Dale, D., and Vian, J., "Real-Time Indoor Autonomous Vehicle Test Environment," *IEEE Control Systems Magazine*, Vol. 28, No. 2, April 2008, pp. 51–64.
doi:10.1109/MCS.2007.914691

[22] Grauer, J., Conroy, J., Hubbard, J., Humbert, J., and Pines, D., "System Identification of a Miniature Helicopter," *Journal of Aircraft*, Vol. 46, No. 4, July–Aug. 2009, pp. 1260–1269.
doi:10.2514/1.40561

[23] Grauer, J., and Hubbard, J., "Experimental Determination of Ornithopter Control Derivatives," AIAA Mid-Atlantic Student Conference, Hampton, VA, AIAA, April 2007.

[24] Grauer, J., and Hubbard, J., "Identification and Integration of Ornithopter Actuator Models," AIAA Atmospheric Flight Mechanics Conference, Chicago, IL, AIAA Paper 2009-5937, Aug. 2009.

[25] Alexander, D., *Nature's Flyers: Birds, Insects, and the Biomechanics of Flight*, Johns Hopkins Univ. Press, Baltimore, MD, 2004, pp. 74–75.

[26] Frampton, K., Goldfarb, M., Monopoli, D., and Cveticanin, D., *Fixed and Flapping Wing Aerodynamics for Micro Air Vehicle Applications*, Progress in Astronautics and Aeronautics, Vol. 195, AIAA, Reston, VA, 2001, pp. 473–482.

[27] Harmon, R., Grauer, J., Hubbard, J., Conroy, J., Humbert, S., Sitaraman, J., and Roget, B., "Experimental Determination of Ornithopter Membrane Wing Shapes used for Simple Aerodynamic Modeling," AIAA Paper AIAA-2008-6237, 2008.

[28] Leishman, J., *Principles of Helicopter Aerodynamics*, Cambridge Univ. Press, Cambridge, England, U.K., 2006, pp. 427–428.

[29] Klein, V., Batterson, J., and Murphy, P., "Determination of Airplane Model Structure from Flight Data Using Modified Stepwise Regression," NASA TP-1916, Oct. 1981.